

Quantum Monte Carlo Study of π -Bonded Transition Metal Organometallics: Neutral and Cationic Vanadium–Benzene and Cobalt–Benzene Half Sandwiches

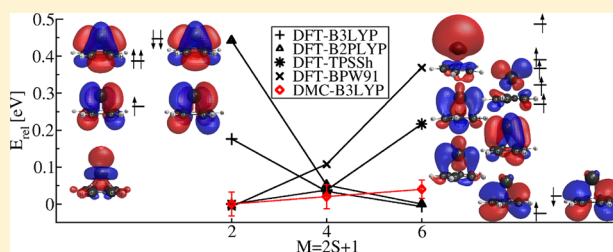
L. Horváthová,[†] M. Dubecký,[†] L. Mitas,[‡] and I. Štich^{*,†}

[†]Institute of Physics, CCMS, Slovak Academy of Sciences, 84511 Bratislava, Slovakia

[‡]North Carolina State University, Department of Physics, Raleigh, North Carolina 27695, United States

S Supporting Information

ABSTRACT: We present accurate quantum Monte Carlo (QMC) calculations that enabled us to determine the structure, spin multiplicity, ionization energy, dissociation energy, and spin-dependent electronic gaps of neutral and positively charged vanadium–benzene and cobalt–benzene systems. From total/ionization energy, we deduce a sextet (quintet) state of neutral (cationic) vanadium–benzene systems and quartet (triplet) state of the neutral (cationic) cobalt–benzene systems. Vastly different energy gaps for the two spin channels are predicted for the vanadium–benzene system and broadly similar energy gaps for the cobalt–benzene system. For this purpose, we have used a multistage combination of techniques with consecutive elimination of systematic biases except for the fixed-node approximation in QMC. Our results significantly differ from the established picture based on previous less accurate calculations and point out the importance of high-level many-body methods for predictive calculations of similar transition metal-based organometallic systems.



1. INTRODUCTION

Complexes of 3d transition metal atoms (TM) and organic molecules belong to an important class of systems that exhibit a number of interesting phenomena such as catalytic properties and strong correlations, which lead to variety of spin and charge states.

The systems of TM atoms (TM = Sc, ..., Ni) bonded with benzene (Bz) represent perhaps the simplest example of bonding between TM and conjugated molecular systems and are of particular interest due to the promising perspectives for spintronics and other applications.¹ Such systems can be experimentally prepared by several methods,^{2,3} including conventional synthetic techniques. Experiments⁴ suggest that the basic structural prototypes appears to be sandwich-type structure $\text{TM}_n^+ \text{Bz}_{n+1}$ for early TMs (Sc...Cr), Figure 1, while for late TMs (Mn...Ni) the most probable structure can be described as a “rice-ball” arrangement where Bz molecules coat

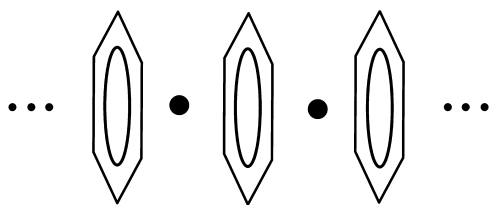


Figure 1. Sandwich-type structure of TMBz complexes with metal atoms separated by benzene molecules.

TM atoms. The basic building component of the sandwich structures is the half sandwich TM_1Bz_1 ; see Figure 1. The sandwich structural patterns can exhibit ferro-antiferromagnetic coupling^{5,6} and therefore can lead to variety of low-lying states with possibly complicated spatial-spin symmetries. Study of these systems is rather demanding on both experimental and theoretical fronts, since the energy differences can be of the order of chemical accuracy (≈ 1 mHa or 0.04 eV). To predict properties of larger systems, such as stacked sandwich-like nanowires, it is crucial to probe thoroughly the electronic and atomic structures of the basic building units (i.e. neutral and cationic TMBz half sandwiches). This is particularly relevant in the light of previous investigations that point out a number of interesting magnetic^{7–9} and transport phenomena.^{5,10} These studies suggest that sandwich-type TM-benzenes could work as spin filters or spin valves, in which the majority spin channel is conductive while the minority spin channel is gapped.¹⁰ There are many more options available for spintronics applications by tuning the properties of stacked structures using length adjustments, termination, and further functionalization of these complexes. In addition, TMBz half sandwiches represent a very simple model for TM–atom adsorption on graphene,^{11–13} which is a vast novel direction in magnetic nanostructures.

Received: October 12, 2012

Published: December 5, 2012

In this study, we focus on four particular members of the TMBz family, namely VBz, VBz⁺, CoBz, and CoBz⁺ half sandwiches as typical representatives of the early- and late-TMBzs, respectively. This work completes our previous effort,¹⁴ which revealed interesting and unexpected features of VBz system as well as sensitivity to the proper treatment of electron correlations. This is crucial, since *d*– π bonded systems show competition of electrostatic, charge transfer, exchange, and correlation effects with variety of possibilities for resulting states including near-degeneracies. Isolated V and Co atoms are both spin quartets, ⁴*F* terms. The question is what happens when their three unpaired 3*d* electrons are docked on the π -bonded Bz molecule. In particular, it is not clear whether the spins moments will be quenched or, possibly, enhanced. Also, it is far from clear what will be the bonding in TMBz systems, since there are several possibilities that can take place between 4*s* and 3*d* levels and Bz conjugate π states. Finally, for the spintronics applications it is crucial to find out the spin gaps in both majority and minority spin channels. Modeling of the larger members of the TMBz family or of systems for spintronic applications, including TM atoms on graphene, will undoubtedly require much larger-scale calculations that would benefit from thorough benchmarking of density functional techniques (DFT).¹⁵ This is particularly important because accurate description of these systems by available DFT methods is not guaranteed a priori. Very serious failures of the DFT methods have been reported in the past, even for apparently much simpler systems. For example, deficiencies of the DFT methods to describe the energetics of small carbons clusters have been identified in the past by QMC methods¹⁶ and, more recently, for organic molecular crystals.¹⁷ Similar DFT deficiencies have been analyzed in QMC studies of TM oxide systems.^{18,19} Very recently, we have used the explicitly correlated QMC methods with the goals to (1) understand the properties of these systems and (2) to benchmark the ability of the various available exchange-correlation (xc) density functionals to describe the complicated *d*– π bond. We have addressed this question by QMC calculations for the VBz system in a recent letter.¹⁴ Transcending this preliminary investigation, here, we not only present a much more extended and comprehensive account of our modeling but also provide novel data for the late TM CoBz/Co⁺Bz systems. Although the QMC calculations are much more demanding computationally, the results enabled us to reveal the DFT biases that are of the order of ≈ 0.5 eV, which is very significant. These biases, most prominent in the less tightly bound neutral species, lead to incorrect energy ordering of the spin multiplets depending on the employed xc-functional.

One may hope to get hints on bonding and properties of the gas-phase TMBz systems from the experimental studies of TMBz complexes,²⁰ including mass spectroscopy,²¹ infrared spectroscopy,²² photoionization (PI),⁴ collision-induced-dissociation (CID),²³ photodissociation,²⁴ Stern-Gerlach molecular-beam magnetic deflection,²⁵ etc. One complication is that most of the experiments probe only the ionic species, one exception being the PI experiments.⁴ There are additional experimental complexities, such as kinetic shifts needed to interpret the CID experiments, or the excited electronic states entering interpretation of the photodissociation experiments. For example, for dissociation energies of half sandwich structures, these factors result in a spread of ≈ 0.5 eV,^{20,23,24,26} even for cations. Additional biases enter when the results from ionic species are extrapolated to neutrals. Similarly, the structures,

even for the smallest cationic half sandwiches including the key TM⁺–Bz distance, have not been experimentally determined. Clearly, there is a need for highly accurate calculations that would cross-validate the existing experimental data as well as predict the quantities that are difficult to obtain in experiments.

On the theoretical side, there are a few studies for cations using correlated approaches based on expansions in basis sets^{27–29} and also density-functional (DFT)^{5–9} calculations for ionic and neutral species. For the more tightly bound cationic half sandwiches quantum-chemical calculations provide complementary information that agrees with experiments quite well for the spin multiplicity and fairly well on the dissociation energy.^{27,29} However, when it comes to neutral TMBz complexes, situation is more complicated.¹⁴ DFT calculations initially suggested that magnetic moments of transition metal atoms embedded in TMBz complexes were increasing from Sc to Cr and decreasing from Mn to Ni in analogy with their behavior when supported on metal surfaces.³⁰ Spin multiplicities of TMBz complexes were predicted to show the same trend and to be enhanced from Sc to Cr and depressed from Cr to Ni compared to spin multiplicities in free atoms.⁷ However, the robustness and reliability of the DFT results for these systems have been undermined by later DFT studies, recent QMC studies,¹⁴ and correlated quantum-chemical studies on related systems,¹¹ which yielded spin multiplicities and dissociation energies different from those found in the previous DFT studies. Taking VBz as an example, spin multiplicities of 2,^{9,12} 4,⁹ and 6^{7,8} and dissociation energies between $\approx 0.7^9$ and ≈ 2 eV^{9,12} were determined using DFT methods, depending on the basis set and treatment used, whereas the QMC results have identified the sextet as the most probable multiplet. In addition, the QMC dissociation energy is ≈ 0.6 eV, suggesting that these properties are very delicate and most likely beyond the capabilities of the standard DFT methods. One could try to improve upon the present treatments by choosing different xc-functionals; however, reliable predictions require very precise benchmarking of any existing biases which is very difficult and ultimately not very efficient since for new type of system the filtering of biases has to be done anew. Alternatively, one can use DFT+U, variety of hybrid functionals or the best available quantum chemistry methods. Correlated wave function methods based on basis sets are viable for describing the trends across the entire TMBz series in the half sandwich structures.¹¹ However, due to the scaling with the system size, it would be hard to extend to the full sandwich structures or beyond. Wehling et al. applied GGA+U methods for the related problem of TM atom adsorption on graphene and found that the results depend qualitatively on the on-site Coulomb repulsion parameter *U*. As shown below, search for appropriate xc-functionals is a daunting task, as even the most recent and sophisticated xc-functionals such as TPSSH^{31,32} or B2PLYP³³ yield inconsistent and conflicting results.¹⁴ Hence, we believe that QMC methods, which combine the accuracy of the best correlated quantum chemistry basis set methods with the favorable scaling provide much needed and valuable alternative to the more traditional approaches.

As we have indicated, previous studies suggest that these systems offer to study a number of interesting magnetic^{7–9} and transport properties,^{3,10} both for applications such as spintronic devices¹⁰ as well as for resolving several more fundamental questions such as behavior of *d*-moments in the presence of conjugated *p*-states and existence of spin gaps in TMBz structures.

In this paper, we perform the most accurate and complete study of neutral and cationic vanadium–benzene and cobalt–benzene half sandwiches by the highly accurate correlated QMC method.^{34,35} The QMC method has a very favorable polynomial scaling with the system size, with accuracy limited only by the choice of the nodal hypersurface of the many-body wave function^{34,35} and the fact that consistent QMC optimization of atomic structures is still a nonstandard procedure. We were able to overcome the difficulties with both these issues for the considered systems. We first test the accuracy of the nodal hypersurfaces on the V^+Bz system where high-quality results by standard quantum chemistry methods exist. This calibration study serves to narrow the number of nodal hypersurfaces, which are then benchmarked. QMC structural optimization, which we were able to employ efficiently by searching only over sensitive degrees of freedom, eliminates the last remaining bias. We, therefore, use the QMC methods to determine the atomic structure, spin multiplicity, ionization energy, dissociation energy, and spin-dependent electronic gaps. Especially for the neutral systems, we find ground-state spin multiplicities and dissociation energies that differ significantly from the previous DFT results. At the same time, our study exposes the shortcomings and biases of the existing experimental results.

The paper is organized as follows. The next section introduces the methods and technical parameters of our calculations. Results for the Vbz^+ , $Cobz^+$ cations, which serve also as a calibration study for narrowing the search for accurate and computationally convenient nodal hyper surfaces for use in the QMC techniques, are in Section 2. The core results of our paper are found in Section 3.2, which summarizes results for the neutral VBz and $CoBz$ complexes. Results for spin-dependent energy gaps are in Section 3.3. More detailed information, such as total (pseudopotential) energies and energies prior to QMC structural optimization, is collected in the Supporting Information (SI). Results for V and Co atoms, V^+ and Co^+ cations, and the Bz system are in Appendices A and B, and the analysis of nodal surfaces are in Appendix C.

2. SIMULATION DETAILS

All simulations used the following five-level refinement strategy, which enabled us to eliminate basically all systematic biases: (1) initial geometries were obtained from DFT optimization, (2) trial wave function was constructed from a truncated CASSCF expansion or from a DFT calculation, (3) trial wave function was optimized using VMC (variational Monte Carlo) techniques, (4) energies were computed from DMC (diffusion Monte Carlo) simulations, and (5) geometry was QMC-optimized focusing on the key $TM-Bz$ distance. For static DFT and CASSCF modeling, we used the GAMESS suite of codes,^{36,37} while all VMC and DMC calculations used the QWalk code.³⁸

The ground-state geometries were initially obtained using DFT techniques spanning all important classes of xc-functionals. We have used the Becke–Perdew–Wang 91 (BPW91)^{39,40} as a representative of a generalized gradient approximation (GGA) xc-functional, Becke–three-parameter–Lee–Yang–Parr (B3LYP)^{41,42} as a representative of a hybrid xc-functional, Tao–Perdew–Staroverov–Scuseria (TPSSH)^{31,32} as a representative of a meta-hybrid functional, Becke–two-parameter–Lee–Yang–Parr (B2PLYP)³³ xc-functional as a representative of a double hybrid functional, and CAM-B3LYP functional⁴³ as a representative of a range-separated xc-

functional. The last three xc-functionals (TPSSH, B2PLYP, CAM-B3LYP) represent “new” type of xc-functionals reported to significantly outperform the “old” type xc-functionals.⁴⁴ The same xc-functionals were also used in the DFT energy calculations and in construction of DFT nodal hypersurfaces for QMC modeling. The only exception being the B2PLYP functional where construction of the corresponding wave function is more intricate. In addition to systematics, use of the BPW91 functional was motivated also by the fact that previous DFT studies of $TMBz$ systems all used the BPW91 functional^{7–9} or the related PBE^{45,46} xc-functional,^{6,12} which makes direct comparison to previous DFT calculations^{6–9} possible. The impact of exact exchange mixing, kinetic energy density, or MP2 correlation can be judged from comparison between B3LYP, TPSSH, B2PLYP, and BPW91 results. The Greeff–Lester type of effective core pseudopotential^{47,48} for all species and cc-pVTZ basis set⁴⁹ were used. In the initial calibration study carried out for the VBz^+ system, various active spaces in the CASSCF method were also used. (4/5) and (10/11) orbital spaces were used for the V^+ cation and (8/13) space for VBz^+ . From CASSCF wave function, natural orbitals, and expansion coefficients were generated. Subsequently, a truncated CASSCF expansion was used retaining all symmetry adapted configuration state functions (CSFs) with weights ≥ 0.01 to construct the variational wave function. Dynamic correlations were explicitly built in via Schmidt–Moskowitz–Jastrow factor,^{35,50} including electron–electron, electron–nucleus, and electron–electron–nucleus correlations. In these multideterminantal trial wave functions,³⁵ the variational parameters, including the weights of the CSFs, were optimized by minimizing linear combination of energy and variance.⁵¹ Alternatively, a single determinant of DFT states was used to determine the nodal part of the trial wave function with parameters of the Jastrow factor optimized. Hence, having in mind the limitations of the previous DFT studies, accurate QMC calculations for these systems have been performed in parallel to the DFT modeling.

The geometry of the $TMBz^+/TMBz$ systems was first determined by a complete DFT optimization of all degrees-of-freedom, whereby we found that the $TM^+-Bz/TM-Bz$ distances are the least robustly determined degrees-of-freedom at the DFT level. Therefore, the structures were QMC-reoptimized focusing on the $TM^+/TM-Bz$ distance. Such an approach is straightforward for a system with symmetry. However, as the symmetry in our systems may be reduced to C_1 with the benzene moiety becoming “wavy” as in the VBz case, the $V-Bz$ distance is more difficult to define. The $TM-Bz$ distance is primarily determined by the $TM-Bz$ bonds. Hence, we define that distance as the average distance over all $TM-C$ distances and the optimization first sets the selected average distance. Then the minimum number of the respective z -coordinates are frozen, namely, those of the V^+/V and of two C atoms, followed by DFT optimization of all the remaining degrees-of-freedom. This process is repeated for different $V^+/V-Bz$ distances, typically in the range ± 0.1 Å, and the minimum determined from the respective DMC energies by a parabolic fit. Such a procedure worked satisfactorily in practice.

3. RESULTS AND DISCUSSION

3.1. Electronic and Atomic Structure of VBz^+ and $CoBz^+$. The VBz^+ cation has extensively been studied by Polestshuk and collaborators,²⁹ who found, using MCQDPT technique, that the system ground-state has a quintet spin multiplicity and spontaneously reduces its symmetry from C_{6h}

($^5A_2(d^3s^1)$ state) to the so-called “up-side-down-boat-shaped” (UDBS) geometry of C_{2v} symmetry ($^5B_2(d^4)$ state), see Figure 2. Quintet spin multiplicity was also found by Bauschlicher et al.²⁷ using MCPF method, who considered C_{6v} symmetry.

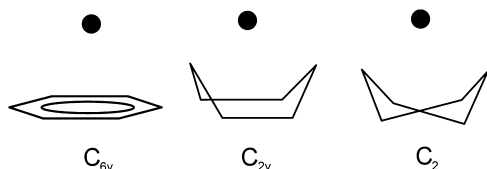


Figure 2. Schematics of the Jahn–Teller distortions in VBz^+ and VBz ; see text for details.

Our energies for VBz^+ in triplet and quintet state, shown in the SI, favor quintet state in UDBS-type of geometry over the triplet state by ≈ 0.2 eV in very good agreement with the MCQDPT result²⁹ of 0.16 eV. In addition, unconstrained minimization under DFT forces also invariably finds the quintet state with the UDBS geometry. We found that the QMC-optimized structures all yield the V^+-Bz distance between 2.38 and 2.41 Å very close to the MCQDPT value of 2.41 Å. The DFT values show somewhat larger spread between 2.35 and 2.42 Å; see the SI. CASSCF(8/13), with orbital space similar to that used in the MCQDPT calculation,²⁹ finds a very shallow minimum at a substantially larger distance of ≈ 2.6 Å. The results of QMC-optimization of the V^+-Bz distance are shown in Figure 3, which clearly show the problem the CASSCF(8/

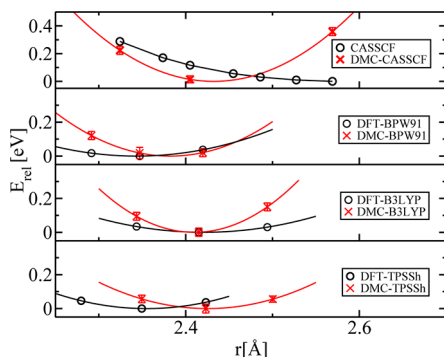


Figure 3. Energies of the VBz^+ system as a function of the V^+-Bz distance. All energies were aligned to zero at the equilibrium V^+-Bz distance in each treatment.

13) method has in describing the $V-Bz^+$ system. The missing dynamical correlations move the minimum to significantly larger V^+-Bz distance of ≈ 2.6 Å, which QMC optimization with CASSCF nodal hypersurfaces reduces back to 2.41 Å, almost identical to the QMC-optimized values with other nodal hypersurfaces and MCQDPT value.²⁹ CASSCF nodal hypersurfaces yield DMC geometry similar to that of MCQDPT. However, the QMC energies, irrespective of DFT nodal hypersurface used, result in V^+-Bz binding energy significantly higher by 0.26 eV than those obtained with DFT nodal hypersurfaces; see the SI.

The calculated V^+Bz adiabatic dissociation energies are summarized in Table 1. The energies do not include the thermal correction, which would increase the dissociation energies by ≈ 0.02 eV.²⁹ Dissociation energies of the fairly tightly bound cationic V^+Bz ($E_0^D \approx 2$ eV) present no serious challenge to the DFT techniques with $E_{0QCH}^D \sim 2.15/2.59$ eV.

Table 1. Adiabatic Dissociation Energy E_0^D ($V^+Bz[M = 3, 5] \rightarrow V^+[^5D] + Bz[^1A_{1g}]$) at Different Levels of Theory^a

Method/Tr. fnct.	M	E_{0QCH}^D	E_{0DMC}^D	E_{0exp}^D
MCQDPT ^b	3	2.21		
DFT B3LYP		1.90	2.05(3)	
DFT BPW91		2.68	2.08(3)	
DFT TPSSH		2.57	2.11(3)	
DFT CAM3BLYP		1.87	2.05(3)	
MP2 ^b	5	2.60		2.31(09) ^e
CCSD(T) ^b		2.53		2.42(10) ^e
MCPF ^c		2.22		2.73(10) ^e
MCQDPT ^b		2.32		2.36, 2.45 ^f
DFT BPW91 ^d		2.63		2.65 ^g
DFT B3LYP ^f		2.16		2.69(22) ^h
CAS-SCF(8/13)			1.93(3)	
DFT B3LYP		2.15	2.30(4)	
DFT BPW91		2.59	2.25(4)	
DFT TPSSH		2.44	2.26(4)	
DFT CAM-B3LYP		2.18	2.16(4)	

^a E_{0QCH}^D labels adiabatic dissociation energies calculated with quantum chemistry methods with wave function used in construction of the trial wave function in calculation of the DMC adiabatic dissociation energies E_{0DMC}^D . E_{0exp}^D are experimental dissociation energies. ^bRef 29. ^cRef 27. ^dRef 7. ^eRef 23. ^fRef 26. ^gRef 20. ^hRef 24.

B3LYP/CAM-B3LYP functionals tend to provide smaller values, whereas BPW91 and TPSSH functionals tend to overbinding. Experiments, photodissociation,²⁰ and collision induced dissociation (CID)^{23,24,26} are of limited guidance as they show a considerable scatter of ≈ 0.4 eV, mainly due to the uncertainties in the kinetic shift applied in the CID experiments.^{23,24,26} DMC dissociation energies E_{0QMC}^D with the different DFT nodal hypersurfaces are within 0.16 eV and very similar to those found by other correlated quantum chemistry methods, MCQDPT and MCPF, which yield 2.32 and 2.22 eV, respectively. Contrary, the DMC with CASSCF nodal hypersurfaces yields dissociation energy lower by ≈ 0.3 eV, indicating that the DMC-CASSCF $V-Bz^+$ energy is too high. We conclude that for a 3d TM system the nodal hypersurfaces constructed from insufficiently correlated single-particle orbitals provide a poor starting point for QMC treatment. Attempts to capture enough correlation energy for construction of a reliable nodal hypersurface by extending the CASSCF orbital space and/or by adding the missing dynamical correlations in perturbative treatment would make the QMC calculation much more involved and computationally intensive. Hence, we conclude that nodal hypersurfaces constructed from DFT orbitals provide computationally convenient and accurate enough framework. For that reason, all other QMC calculations will be using the DFT nodal hypersurfaces. Similar conclusion in the realm of systems with TM atoms was made also previously.⁵² In summary, our best DMC energies, together with results of other highly correlated quantum chemistry results,^{27,29} provide a strong indication that the dissociation energy of the $V-Bz^+$ is somewhat lower than the experimental values, all featuring basically the same experiment with different kinetic shifts.^{23,24,26}

Unlike for V^+Bz , where the $M = 3$ and $M = 5$ states are within ≈ 0.2 eV degenerate, for Co^+Bz , the $M = 3$ state is favored over the $M = 5$ state by more than 1 eV; see the SI. The DFT and QMC adiabatic dissociation energies are shown in Table 2. The trends are similar to those observed for V^+Bz . B3LYP/CAM-

Table 2. Adiabatic Dissociation Energy E_0^D ($\text{Co}^+\text{Bz}[M = 3, 5] \rightarrow \text{Co}^+[\text{}^3\text{F}] + \text{Bz}[\text{}^1\text{A}_{1g}]$) at Different Levels of Theory

Method/Tr. fnct.	M	$E_{0\text{QCH}}^D$	$E_{0\text{DMC}}^D$	$E_{0\text{exp}}^D$
MCPF ^a	3	2.71		
DFT BPW91 ^b		3.91		
DFT B3LYP ^d		2.65		2.54(10) ^c
DFT B3LYP		2.60	2.85(4)	2.65(10) ^c
DFT BPW91		3.34	2.82(4)	2.71, 2.78 ^d
DFT TPSSh		3.25	2.87(4)	2.65 ^e
DFT CAM-B3LYP		2.77	2.82(4)	2.95(22) ^f
DFT B3LYP	5	1.53	1.68(3)	3.07(10) ^c
DFT BPW91		1.57	1.68(3)	
DFT TPSSh		1.79	1.73(3)	
DFT CAM-B3LYP		1.55	1.74(3)	

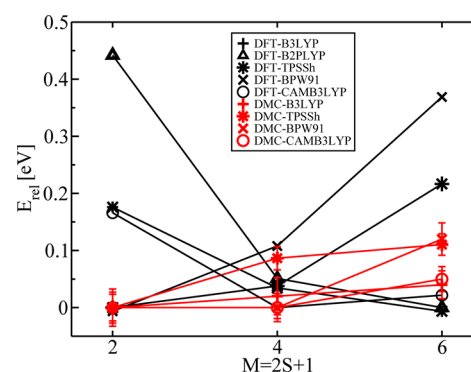
^aRef 27. ^bRef 7 and 8. ^cRef 23. ^dRef 26. ^eRef 20. ^fRef 24.

B3LYP DFT energies tend to underbind whereas BPW91 and TPSSh show tendency to overbinding. DMC energies, irrespective of the DFT hypersurface used yield to within chemical accuracy dissociation energies of 2.8 eV. Uncertainties in kinetic energy shifts in CID methods render the experimental results of only qualitative value.

3.2. Electronic and Atomic Structure of VBz and CoBz.

The first most important preliminary is to determine the spin multiplicity. We have considered three multiplicities of VBz, namely, 2, 4, and 6. All three multiplicities have been considered in the DFT framework by Pandey et al.,^{7–9} and the ground-state multiplicity has been several times revised. Our DFT optimized energies for both functionals, along with the key TM–Bz distances, are summarized in the SI. Using symmetry unconstrained optimization, we found that for $M = 2$ the system keeps the C_{2v} symmetry. For $M = 4$, the system lowers the energy by lowering the symmetry from C_{2v} to C_1 . However, in practical terms, this geometry is very similar to the zigzag C_2 geometry; see Figure 2. For $M = 6$, the symmetry is further reduced to C_1 resulting in a “wavy” configuration of Bz with the V atom moving away from the center of the Bz ring. The symmetry reduction, while small in geometrical terms, reduces the DFT energies by up to ≈ 0.2 eV. The increase of the spin multiplicity is accompanied by a systematic increase in the V–Bz distance from 2.09 Å for $M = 2$ to 2.45 Å for $M = 6$. The bias in the bond lengths from the DFT functionals is significant. It is caused by the interplay of various terms and the bond lengths can be qualitatively correlated with the tendency to overbind/underbind. Taking the hybrid B3LYP (exact exchange mixing percentage 20%) and TPSSh (mixing percentage 10%) as examples, we find that the underbinding B3LYP functional increases the V–Bz distance by up to 0.06 Å in comparison with the overbinding TPSSh functional. The QMC optimized bond lengths also show a mild influence of the exact exchange mixing in the functionals used to generate the orbitals. Finally, and most importantly, the five DFT xc-functionals tested (BPW91, B3LYP/CAM-B3LYP, TPSSh, and B2PLYP) make opposite predictions as to the ground-state spin multiplicity; see Figure 4. B3LYP/CAM-B3LYP and B2PLYP predict VBz to be spin sextet by a large energy margin of ~ 0.4 eV, whereas BPW91 and TPSSh xc-functionals predict it to be spin doublet by about the same energy margin.

Proper account of correlation at the DMC level after structural optimization, Figure 4, finds qualitatively very different picture from DFT in that the energy differences are globally reduced by a factor of 5 with respect to DFT. All

**Figure 4.** Energies of the neutral VBz for spin multiplicities $M = 2, 4, 6$ calculated in DFT and DMC approaches. The values are relative to the lowest found energy.

energies are now degenerate to within ≈ 0.1 eV. Basically, the results fall into two categories depending on the DFT nodal hypersurface used. B3LYP and CAM-B3LYP yield almost identical results with degenerate energies within the error bars for the three multiplicities. For $M = 6$, BPW91 and TPSSh xc-functionals yield very similar results with energies disfavoring high spin multiplicity by a margin of ≈ 0.1 eV. For $M = 4$, the DMC energies obtained with the two nodal hypersurfaces differ somewhat on the ≈ 0.1 eV energy scale with TPSSh nodal hypersurface leading to degenerate energies, whereas BPW91 nodal hypersurface leading to energy larger by ≈ 0.1 eV. At this point, we conclude that DMC energies yield essentially degenerate energies at the energy scale of ≈ 0.1 eV and it is not possible to decide which spin multiplicity will be realized in reality based on total energy only.

To discriminate between the different almost degenerate spin-multiplicities we calculate the vertical ionization potentials IP for each multiplicity. The results are listed in Table 3 along with experimental values and other calculations. We find that, irrespective of the DFT nodal hypersurface used, the DMC IPs calculated in $M = 6$ multiplicity are in slightly better agreement, to within ≈ 0.1 eV, with the experimental value than for the other spin multiplicities. The DFT IPs, except of B2PLYP results, are similarly close to the experimental value of 5.11 eV, hence of comparable quality to the DMC results. We assume that this is a fortuitous error cancellation, as similar underbinding (B3LYP) or overbinding (BPW91) affects both the cation and the neutral VBz. All other multiplicities yield results in worse agreement with the experiment. Given the near degeneracy of the different spin multiplicities, one can speculate that the VBz half sandwich may coexist in a mixture of spin states. If indeed true, such an assumption would only improve agreement between our calculations and photoionization experiments; see Table 3. We conclude that the most probable spin multiplicity is spin sextet. High spin state is also in agreement with the high spin-state of the cation; see Section 3.1. Comparison based on IPs is a very stringent test, as the vertical ionization energies are experimentally directly and accurately measurable. The spin states could directly be deduced from the Stern–Gerlach molecular-beam magnetic deflection experiments,²⁵ which are *not* available for the VBz half sandwich.

We find staggering dissociation energy differences between the different DFT functionals (see Table 3) with B3LYP/B2PLYP underbinding by a factor of 2–3 and BPW91 and TPSSh overbinding by the same factor with respect to our

Table 3. Adiabatic Dissociation Energy E_0^D ($\text{VBz}[M = 2, 4, 6] \rightarrow \text{V}^4\text{F} + \text{Bz}[^1\text{A}_{1g}]$) and Vertical Ionization Potential IP of VBz Calculated at Different Levels of Theory^a

Method/Tr. fct.	M	$E_{0\text{QCH}}^D$	$E_{0\text{DMC}}^D$	$E_{0\text{exp}}^D$	IP _{QCH}	IP _{DMC}	IP _{exp}
MR-CI ^b	4	0.11, 0.03					
DFT BPW91	2, ^c 4, ^e 6 ^{d,c}	0.67, ^c 0.81, ^{e,d} 2.09 ^c			5.53		
DFT B3LYP	2	0.17	0.65(5)		5.53	5.61(4)	
DFT BPW91		1.92	0.65(4)		5.79	5.61(4)	
DFT TPSSh		1.57	0.77(3)		4.53	5.69(3)	
DFT CAM-B3LYP		0.22	0.66(3)	0.67(10) ^f	5.44	5.57(3)	
DFT B2PLYP		−0.29		0.78(11) ^f	4.54		
DFT B3LYP	4	0.31	0.63(5)	1.09(11) ^f	5.25	5.37(3)	
DFT BPW91		1.80	0.65(4)	0.72, 0.81 ^g	5.48	5.38(3)	5.11(4) ^j
DFT TPSSh		1.53	0.67(3)	1.01 ^h	5.21	5.26(4)	
DFT CAM-B3LYP		0.39	0.65(3)	1.05(22) ⁱ	5.32	5.26(4)	
DFT B2PLYP		0.12			5.19		
DFT B3LYP	6	0.35	0.61(5)		4.97	5.01(4)	
DFT BPW91		1.54	0.53(4)		5.21	4.95(4)	
DFT TPSSh		1.35	0.64(3)		4.99	5.01(3)	
DFT CAM-B3LYP		1.35	0.60(3)		4.99	4.94(4)	
DFT B2PLYP		0.15			4.99		

^a $E_{0\text{QCH}}^D/\text{IP}_{\text{QCH}}$ labels dissociation energies/ionization potentials calculated with quantum chemistry methods with wave function used in construction of the trial wave function in DMC calculation of the dissociation energies/ionization potentials $E_{0\text{DMC}}^D/\text{IP}_{\text{DMC}}$. The values correspond to energies obtained after QMC optimization of the V–Bz distance. $E_{0\text{exp}}^D/\text{IP}_{\text{exp}}$ are experimental dissociation energies/vertical ionization potential. ^bRef 28. ^cRef 9. ^dRef 7. ^eRef 8. ^fRef 23. ^gRef 26. ^hRef 20. ⁱRef 24. ^jRef 4.

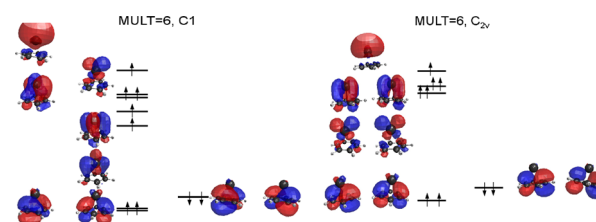
DMC values of ≈ 0.60 eV which turn out to be very robust and only weakly dependent on the xc-functional used to construct the nodal hypersurfaces. However, our DFT calculations do not reproduce the previous DFT studies^{7–9} that find dissociation energies between 0.67 and 2.09 eV, even if we use the same xc-potential. These differences arise most likely due to a combination of smaller basis sets and use of high-symmetry structures in the previous studies. Experiments yield dissociation energies between 0.67 and 1.05 eV; see Table 3. However, unlike ionization potentials, the adiabatic dissociation energies are experimentally only indirectly estimated for neutral species from the relation^{4,7–9}

$$D(\text{TMBz}) = D(\text{TMBz}^+) + \text{IP}(\text{TMBz}) - \text{IP}(\text{TM})$$

where $D(\text{TMBz}^+)$ is adiabatic dissociation energy of the cationic TMBz, and $\text{IP}(\text{TMBz})$ and $\text{IP}(\text{TM})$ are vertical ionization potentials of TMBz and TM atom, respectively. Such a formula would only be strictly valid if adiabatic ionization potentials were used. Hence, using this formula in combination with experimentally biased dissociation energies of the cation (see Section 3.1), a significant bias is to be expected.

Can these findings of preference for a high spin-state and symmetry lowering be understood in simple physical terms? Some aspects of the stabilization can be recognized already at the single-particle level. For that reason, we turn to B3LYP DFT, which yields results in reasonable qualitative agreement with the correlated QMC results. As an example, let us discuss the symmetry lowering of the high-spin state structure $M = 6$. In Figure 5, we show nine MOs highest in energy for C_1 and C_{2v} structures of the spin sextet state. Simple counting of bonding and antibonding MOs reveals that there are two antibonding MOs in C_1 geometry, compared to three in C_{2v} symmetry, which accounts for the stabilization of the lower symmetry structure. Similar arguments explain also the preference for a high spin state.

The next question that we encounter is whether the deficiencies of the DFT techniques identified above are limited

**Figure 5.** DFT B3LYP molecular orbital picture of bonding in VBz along with schematic position of the orbital energies in spin multiplicity $M = 6$. (Left) C_1 symmetry, (right) C_{2v} symmetry.

to the neutral VBz and caused by the near degeneracy of the different spin multiplets in this system. For cationic TMBz half sandwiches, we have observed near degenerate $M = 3$ and $M = 5$ multiplets in V^+Bz , whereas the same multiplets were separated by ≈ 1 eV in Co^+Bz system. Hence, here, we study the neutral CoBz system to compare with the VBz. The first observation is that, contrary to what we found in VBz, in CoBz the structure always retains C_{2v} symmetry, irrespective of the spin multiplicity. However, the Co–Bz distance increases from ≈ 2.05 Å for $M = 2$ to ≈ 2.45 Å for $M = 6$ for each xc-functional, except for B2PLYP (see the SI) in analogy with VBz. The absolute total pseudopotential energies are summarized in the SI, the relative energies of the $M = 2, 4$, and 6 spin multiplets are shown in Figure 6. In CoBz, the $M = 6$ high-spin state is strongly energetically disfavored by ≈ 2 eV, a feature correctly captured by all xc-functionals considered. The more subtle energy differences between the $M = 2$ and $M = 4$ multiplets again show controversies in the DFT description. BPW91 yields the $M = 2$ state as the ground-state by a ≈ 0.2 eV margin, TPSSh predicts near degeneracy of the two states, and B2PLYP and B3LYP/CAM-B3LYP overestimate the energy differences of the two multiplets by about a factor of 2. On the contrary, DMC energies, irrespective of the nodal hypersurface employed, show only small variations within their respective error bars and clearly favor the $M = 4$ spin multiplet.

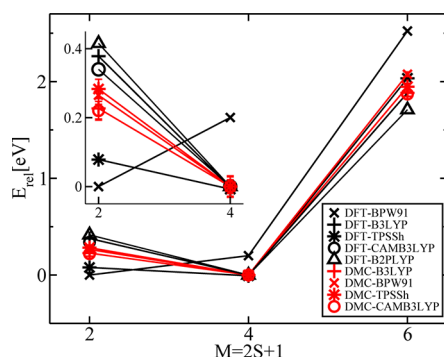


Figure 6. Energies of the neutral CoBz calculated for spin multiplicities $M = 2, 4, 6$ calculated in the DFT and DMC approaches. Other details as in Figure 4.

Computed adiabatic dissociation energies E_0^D for CoBz are compiled in Table 4. The most prominent feature of the DFT results are the negative E_0^D values we observe for all three multiplicities. Taking the ground-state $M = 4$ as example, B3LYP/CAM-B3LYP and B2PLYP all yield negative E_0^D values, whereas TPSSH and BPW91 yield overbinding by factors of 2 and 3, with respect to DMC values, respectively. On the other hand, DMC-estimated E_0^D values are all ≈ 0.3 eV, irrespective of the nodal hypersurface. The negative E_0^D values for the ground-state multiplet are likely manifestation of multireference character of this system. The experimental estimates of the dissociation energies suffer from the biases mentioned already in the case of VBz and predict energies between ≈ 0.2 and ≈ 0.7 eV; hence, they form barely stable species up to bond strength similar to VBz.

Comparing our results for TMBz to other computational studies, we were not able to reproduce some of the previous BPW91 DFT results.^{7–9} Recently adsorption of both vanadium and cobalt atoms on graphene and benzene was studied using orbital-corrected PBE functional,¹² and an equal moment of $1 \mu_B$ for adsorption of both V and Co on benzene was proposed. Given the similarity between BPW91 and PBE xc-functionals, such a conclusion is in agreement with our DFT-BPW91 results, but it disagrees with results of other xc-functionals and

QMC results. On the other hand, our DMC results agree very well with results of ref 11, which studied, using CASPT2 approach, adsorption of a Co atom on coronene as an approximant to graphene which finds $M = 4$, $E_0^D \approx 0.3$ eV. On the other hand, it is not clear why the MR-CI calculation²⁸ for neutral VBz half sandwich yields results in total disagreement with both experiments and all other theories; see Table 3.

Comparing our QMC results for the early TM VBz system to the late TM CoBz system, we conclude that putting 4F vanadium atom onto benzene results in amplification of the spin of the resulting complex from $3/2$ to $5/2$ and an appreciable bond strength of ≈ 0.65 eV. On the contrary, putting a 4F cobalt atom onto a benzene molecule results in conservation of the $3/2$ spin of the atom also in the complex and a much weaker Co–Bz chemical bond of ≈ 0.3 eV.

3.3. Spin-Dependent Gaps in VBz and CoBz. Due to the unpaired spins and spin-dependent gaps, TMBz sandwiches have been proposed as prospective spin valve spintronic units. Having this motivation in mind, we have calculated the gaps also for the VBz and CoBz half sandwiches. Within the DFT framework, we present the HOMO–LUMO gaps, which are straightforward to calculate. Since a HOMO–LUMO gap is a single-particle concept the excitations in the many-body QMC, we calculate the gap as differences between the total energies³⁴ as follows

$$E_g^{\uparrow,\downarrow} = (E_{N+1}^{\uparrow,\downarrow} - E_N) - (E_N - E_{N-1}^{\uparrow,\downarrow})$$

The results for HOMO–LUMO and QMC gaps for the spin sextet case of VBz and spin quartet state of CoBz are in Tables 5 and 6, respectively. We indeed see that for VBz the majority spin gap is about half of that for the spin minority gap and that the DFT HOMO–LUMO gaps are again roughly half of the optical gaps. The difference between the spin-majority/spin-minority gaps is expected to increase with the sandwich length.¹⁰ This behavior differs again in CoBz, where the QMC gaps in the two spin populations are broadly similar.

4. SUMMARY AND CONCLUSIONS

In summary, we have carried out a study of neutral and positively charged vanadium–benzene and cobalt–benzene

Table 4. Adiabatic Dissociation Energy E_0^D ($\text{CoBz}[M = 2, 4, 6] \rightarrow \text{Co}[^4F(3d^7 4s^2)] + \text{Bz}[^1A_{1g}]$) and Vertical Ionization Potential IP of CoBz Calculated at Different Levels of Theory

Method/Tr. funct.	M	$E_{0\text{QCH}}^D$	$E_{0\text{DMC}}^D$	$E_{0\text{exp}}^D$	IP _{QCH}	IP _{DMC}	IP _{exp}
DFT BPW 91 ^{a,b}	2	3.91			5.94		
DFT B3LYP	2	−0.58	0.08(2)		5.01	5.14(4)	
DFT BPW91		1.24	0.13(2)				
DFT TPSSH		0.61	0.04(2)		5.26	5.18(4)	
DFT CAM-B3LYP		−0.38	0.08(2)				
DFT B2PLYP		−0.74					
DFT B3LYP	4	−0.20	0.30(2)	0.21(11) ^c	5.35	5.40(4)	
DFT BPW91		1.04	0.40(2)	0.32(11) ^c	5.43		
DFT TPSSH		0.70	0.34(2)	0.38, 0.45 ^d	5.29	5.23(4)	5.55(4) ^g
DFT CAM-B3LYP		−0.04	0.30(2)	0.32 ^e	5.26		
DFT B2PLYP		−0.30		0.62(22) ^f	6.82		
DFT B3LYP	6	−2.08	−1.58(2)	0.74(10) ^c	3.82	3.97(4)	
DFT BPW91		−1.28	−1.67(2)				
DFT TPSSH		−1.34	−1.62(2)		3.80	3.84(4)	
DFT CAM-B3LYP		−1.91	−1.57(2)				
DFT B2PLYP		−2.01					

^aRef 7. ^bRef 8. ^cRef 23. ^dRef 26. ^eRef 20. ^fRef 24. ^gRef 4.

Table 5. Spin-Dependent Optical Gaps $E_g^{\uparrow,\downarrow}$ and HOMO–LUMO Gaps in VBz in Spin Sextet State

method	E_g^{\uparrow} eV	E_g^{\downarrow}
DMC/B3LYP	4.90	10.04
DMC/TPSSH	5.19	9.68
DFT/B3LYP	4.65	9.44
DFT/TPSSH	5.10	9.26
HOMO–LUMO (B3LYP)	2.34	6.28
HOMO–LUMO (TPSSH)	1.30	5.56

Table 6. Spin-Dependent Optical Gaps $E_g^{\uparrow,\downarrow}$ and HOMO–LUMO Gaps in CoBz in Spin Quartet State

method	E_g^{\uparrow} eV	E_g^{\downarrow}
DMC/B3LYP	6.22	7.12
DMC/TPSSH	6.08	7.28
DFT/B3LYP	6.24	7.19
DFT/TPSSH	6.14	7.54
HOMO–LUMO (B3LYP)	2.40	4.03
HOMO–LUMO (TPSSH)	1.79	3.79

organometallic complexes using explicitly correlated QMC methods. These calculations involved also QMC geometry optimizations and a multistage strategy to eliminate basically all systematic biases except the fixed-node error. Although the QMC calculations are much more demanding computationally, the results enabled us to reveal a number of interesting properties of TMBz systems and also provided new data for benchmarking quality of DFT calculations and their inconsistencies, as well as to reveal genuine DFT biases. For the more tightly bound cationic systems, our QMC results confirm the previous DFT and results obtained by correlated quantum chemical calculations based on basis sets. However, for the much less tightly bound neutral species, we found incorrect and varying energy ordering of spin multiplets depending on the employed functional. In particular, the vanadium–benzene system rather unexpectedly exhibits quasi-degenerate energies of the various spin multiplets despite the fact that a number of tested DFT functionals show varying differences of the order of a few tenths of an electronvolt. This is very significant considering the true spin-flip energies that are typically of the same magnitude. Furthermore, we were able to determine accurate values of ionization energies that could be used to consistently identify the states of interest in theory and experiment using accurate values of ionization energies. From the total energies/ionization energies, we have concluded that the most probable ground state of the vanadium–benzene is the spin sextet, whereas for cobalt–benzene we find the spin quartet ground state directly from the total energies. Our calculations illustrate the scatter and significant differences of DFT dissociation energies, which sensitively depend on the used xc-functional. On the contrary, very similar QMC dissociation energies were obtained for several types for wave functions based both on DFT and correlated quantum-chemical approaches with only very weak dependence on the resulting nodal hypersurfaces. Overall, the B3LYP xc-functional appears to be consistently closest to QMC results and, vice versa, its nodal hypersurfaces yield the QMC results closest to experiments. CAM-B3LYP results and nodal hypersurfaces are almost indistinguishable from B3LYP, except for VBz where

CAM-B3LYP leads to incorrect $M = 4$ multiplicity, albeit by only a small margin. BPW91 appears to spuriously favor the low-spin multiplicity, as does the TPSSH xc-functional, both featuring surprisingly similar nodal hypersurfaces. We have calculated spin gaps that are of interest for spintronics applications. Interestingly, we find vastly different energy gaps for the two spin populations in vanadium–benzene, whereas in cobalt–benzene the two spin gaps are found to be broadly similar. The QMC errors arising due to use of the different DFT nodal hypersurfaces are consistently within ≈ 0.1 eV. While this is still above the elusive chemical accuracy, QMC reduces the errors in the energy differences between the spin multiplets are smaller by a factor of ≈ 5 . The QMC dissociation energies point toward possible inaccuracies in the corresponding experimental values. These calculations offer not only new insights into the transition metal–benzene systems and their cations but open new opportunities for using QMC methods for many other organometallic systems, such as, for instance, TM–graphene magnetic nanostructures.

■ APPENDIX A: ELECTRONIC STRUCTURE OF V, V⁺, AND CO, CO⁺

The dissociation processes of interest here, $\text{TmBz}^+ \rightarrow \text{Tm}^+ + \text{Bz}$ and $\text{TmBz} \rightarrow \text{Tm} + \text{Bz}$ lead to dissociation into V⁺ and V fragments, respectively. Unlike Bz, which is very easy to describe accurately (see Appendix B and the SI), the V/Co atom and cation represent a complicated TM system with partially filled *d*-shell with a competition between *d* and *s* electrons. Hence, low-lying excitations in the spectrum of a single atom are composed of $3d \leftrightarrow 4s$ transitions. For example, the 5D term with $3d^4$ configuration in V⁺ is only 0.34 eV below the 5F term of V⁺ with $3d^3 4s^1$ configuration⁵⁵ or the 4F terms with $3d^7 4s^2$ and $3d^8 4s^1$ configurations in Co are only 0.44 eV apart. This fact violates the Hund's rule and suggests that the correlation is crucial for these states so that the many-body treatment is necessary. The $3d/4s$ competition is present also in TM complexes. However, in the complexes occupation of the *4s* shell is counteracted by Pauli repulsion between the ligand and *4s* electrons. Therefore, it is important to account for the interplay between different electronic states. For example, the experimental dissociation energies of $\text{CoBz}^+ \rightarrow \text{Co}^+ + \text{Bz}$ is in the range 2.54–3.07 eV^{23,24,26} but only 0.21–0.74 eV for CoBz .^{23,24,26} Furthermore, the atomic and ionic terms may require two determinants in real representation to correctly describe the space-spin symmetries. Hence, the ability to compute energies of the atomic/ionic fragments accurately, is of paramount importance.

The total energies computed for the 5D and 5F terms of V⁺ and 4F term of V are summarized in the SI. The DMC energies computed with CASSCF nodal hypersurfaces are always higher than those computed with DFT nodal hypersurfaces, albeit by small margins. The only exception is the 5D term of V⁺, where CASSCF(10/11) yielded nodal hypersurfaces of the lowest DMC energy. In all the other cases, the DFT theory, irrespective of the xc-potential used, yielded nodal hypersurfaces that lead to DMC energies lower by ≈ 0.08 eV (5F) and ≈ 0.18 eV (4F) than the CASSCF nodal hypersurfaces. This is a strong indication that construction of accurate nodal hypersurfaces starting from uncorrelated Hartree–Fock orbitals is not easy in systems containing TM atoms. In this respect, the DFT techniques, correlated already at the single-particle level, appear to be much more accurate and also economical way to describe the TM systems. The same conclusion was reached in the case

of V^+Bz complex; see Sect. 3.1 and earlier in the context of TM–oxide solids^{18,19} and molecules.⁵² This finding is at variance with the simpler π -bonded systems where CASSCF nodal hypersurfaces provided a very accurate ansatz for the determinantal part of the trial wave function for both ground- and excited-states.^{57,58}

The computed transition/ionization energies for V/V^+ are shown and compared with experimental results and results of other computations in Table 7. Surprisingly, not only CASSCF

Table 7. $^5D \rightarrow ^5F$ Excitation Energy of the V^+ Cation and $^4F \rightarrow ^5D$ Ionization Energy of V atom Calculated at Different Levels of Theory^a

excitation	Method/Tr. fnct.	ΔE_{QCH}	ΔE_{DMC}	$\Delta E_{exp}^{\ddagger}$
$^5D \rightarrow ^5F$	MP2 ^b	0.08		0.34 ^e
	CCSD(T) ^b	−0.07		
	CAS-SCF(4/5) ^b	−0.38		
	MCQDPT ^b	0.21		
	CASSCF(4/5(6))	−0.43	0.30(2)	
	CASSCF(10/11)	−1.28	0.41(2)	
	DFT B3LYP	0.28	0.23(2)	
	DFT BPW91	0.55	0.23(2)	
	DFT TPSSh	0.53	0.23(1)	
	DFT CAM-B3LYP	0.37	0.27(2)	
	FCI/MRSDCI ^f	6.78		6.75 ^e
	ACPF/CBS ^c	6.73		
	CISD(T) ^d	6.84		
	CASSCF(4/5)	6.13	6.47(2)	
$^4F \rightarrow ^5D$	CASSCF(10/11)	7.13	6.33(2)	
	DFT B3LYP	6.77	6.64(2)	
	DFT BPW91	6.23	6.62(2)	
	DFT TPSSh	6.22	6.60(1)	
	DFT CAM-B3LYP	6.71	6.58(2)	

^a E_{QCH} labels energies calculated with quantum chemistry methods with wave function used in construction of the trial wave function in calculation of the DMC energies E_{DMC} . All energies in eV. ^bRef 29. ^cRef 53. ^dRef 54. ^eRef 55; *j*-averaged value. ^fRef 56.

and MP2 but also the CCSD(T) method find incorrect ground-state, 5F , of V^+ . This is, most likely, due to the multireference character of the V^+/V . DMC manages to correct the order of the 5D , 5F states from the CASSCF method. Surprisingly, DFT yields correct ordering of the energies, irrespective of the xc-functional used, albeit with a large difference in energies. B3LYP/CAM-B3LYP, which slightly underestimate the energy differences, is significantly more accurate than BPW91 and TPSSh, which largely overestimate the energy differences by over 50%. DMC energies are fairly resistant to the fine details of the nodal hypersurfaces. In particular, the 5D , 5F DMC energy difference of ≈ 0.23 eV is very similar to the MCQDPT value of 0.21 eV.²⁹ Similar conclusion is reached for the ionization potential ($^4F \rightarrow ^5D$ process), where again DMC energies are a definite improvement over the CASSCF energies but improve only on the BPW91 and TPSSh energies. DMC energy differences for all DFT nodal hypersurfaces are surprisingly similar, ≈ 6.60 eV. At the DFT level, the B3LYP/CAM-B3LYP results are again significantly better than both BPW91 and TPSSh results, which are underestimating the energy difference by ≈ 0.5 eV.

Total energies computed for the $^3F(3d^8)$ and $^5F(3d^74s^1)$ terms of Co^+ and $^4F(3d^74s^2)$ and $^4F(3d^84s^1)$ terms of Co are summarized in the SI. Energies of the corresponding $^3F \rightarrow ^5F$,

$^4F \rightarrow ^4F$ transitions in Co^+ and Co, respectively, and the $^4F \rightarrow ^3F$ ionization energy is summarized in Table 8 along with

Table 8. $^3F(3d^8) \rightarrow ^5F(3d^74s^1)$ and $^4F(3d^74s^2) \rightarrow ^4F(3d^84s^1)$ Excitation Energy of the Co^+ Cation and Co Atom, Respectively, and $^4F(3d^74s^2) \rightarrow ^3F(3d^8)$ Ionization Energy of Co Atom Calculated at Different Levels of Theory

excitation	Method/Tr. fnct.	ΔE_{QCH}	ΔE_{DMC}	ΔE_{exp}
$^4F \rightarrow ^4F$	MCPF ^a	0.30		0.41 ^f
		−0.10		
	CISD(T) ^c	0.58		
	DFT B3LYP	0.28	0.44(3)	
	DFT BPW91	0.33	0.37(2)	
$(3d^74s^2) \rightarrow (3d^84s^1)$	DFT TPSSh	0.15	0.44(2)	
	CAM-B3LYP	0.30	0.42(2)	
	MCPF ^a	0.70		0.44 ^f
		1.03		
	ACPF/CBS ^b	0.51		
$^3F \rightarrow ^5F$	CASPT2 ^c	0.38		
	DFT B3LYP	0.68	0.62(1)	
	DFT BPW91	0.88	0.70(2)	
	DFT TPSSh	0.79	0.64(2)	
	CAM-B3LYP	0.74	0.62(2)	
$^4F \rightarrow ^3F$	ACPF/CBS ^b	7.94		7.88 ^f
	CISD(T) ^d	8.03		
	DFT B3LYP	8.05	7.80(2)	
	DFT BPW91	7.64	7.70(2)	
	DFT TPSSh	7.77	7.74(2)	
$(3d^74s^2) \rightarrow (3d^8)$	CAM-B3LYP	8.00	7.78(2)	

^aRef 59 nonrelativistic/relativistic. ^bRef 53. ^cRef 11. ^dRef 54. ^eRef 60. ^fRef 55; *j*-averaged value.

experimental data and selected theoretical values. DFT is overestimating the $^3F \rightarrow ^5F$ energy, by a factor of ≈ 2 with DMC values representing a $\approx 30\%$ improvement with respect to experiment. On the contrary, all DFT values of the $^4F \rightarrow ^4F$ transition are significantly underestimated, for TPSSh by as much as $\approx 80\%$, with DMC values being within chemical accuracy from the experimental values. All dissociation energies (DFT, DMC) are fairly good in DFT description and ≈ 0.1 eV smaller in DMC description.

■ APPENDIX B: ELECTRONIC STRUCTURE OF BENZENE

Benzene is the other dissociation fragment needed for calculation of dissociation energies. The results for benzene energies calculated with different quantum chemistry and QMC methods (D_{6h} symmetry, $^1A_{1g}$ state) are shown summarized in the SI. While energies from quantum chemistry methods differ appreciably, with the CASSCF energy being as much as ≈ 1 Ha higher than the DMC energy, the DMC energies obtained from nodal hypersurfaces from those methods differ by at most 0.03 eV. The finding that the static and dynamical correlations are well separated in simple π -bonded systems has been found previously.^{57,58} Hence, CASSCF energies, lacking dynamical correlations, provide poor energies but describe well the nodal hypersurfaces in simple π -bonded systems.

■ APPENDIX C: CHARACTERIZATION OF NODAL HYPERSURFACES

In Section 3.2, we argued that the different DFT xc-functionals found incorrect and varying energy ordering of spin multiplets depending on the employed xc-functional. B3LYP and BPW91 xc-functionals provided typically the most different orderings, with spin sextet of VBz being the most striking example; see Figure 4. To better understand those differences, we now directly compare the underlying B3LYP and BPW91 nodal hypersurfaces. We note that the QMC energies are critically dependent on the nodal hypersurfaces. To this end, we use the procedure of direct stochastic “measuring the differences between nodal hypersurfaces”, ΔS_{node} , as outlined in ref 57. Similarly, differences between a pair of nodal surfaces can be quantified using the value of coefficient of the falloff ξ_1 in the fitting function $y = \xi_0 \exp(-\xi_1 x)/(x)^{1/357}$ used to approximate the difference of the distributions of the nodal hypersurfaces. The distribution of differences between the B3LYP and BPW91 nodal hypersurfaces, ΔS_{node} , for all three spin multiplicities calculated on a B3LYP-optimized structure is shown in Figure 7. We indeed find that the BPW91 nodal hypersurface differs

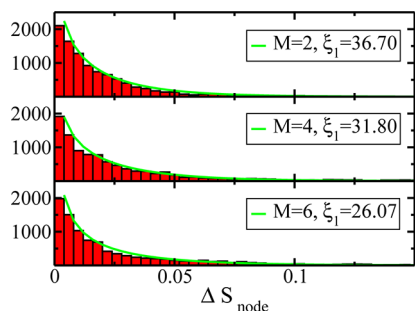


Figure 7. Distribution of the differences between B3LYP and BPW91 nodal hypersurfaces (red histogram)⁵⁷ for spin multiplicities $M = 2, 4$, and 6 . Green lines are histogram fits with $y = \xi_0 \exp(-\xi_1 x)/(x)^{1/3}$ function.⁵⁷.

most from the B3LYP hypersurface in the spin sextet case where $\xi_1 \approx 26$, whereas it differs least in the case of a doublet, where $\xi_1 \approx 37$. This finding indicates that the results for high-spin states are more vulnerable compared to the results for low-spin states.

For $M = 6$ in VBz, results cluster into two groups. B3LYP/CAM-B3LYP and BPW91/TPSSH provide very similar predictions both at DFT and QMC level; see Figure 4. The distributions of differences between the B3LYP and CAM-B3LYP and BPW91 and TPSSH nodal hypersurfaces, ΔS_{node} , for $M = 6$, are shown in Figure 8. As evidenced by the large value of $\xi_1 \approx 58$, the B3LYP and CAM-B3LYP nodal hypersurfaces are indeed very similar. The BPW91 and TPSSH nodal hypersurfaces exhibit a falloff coefficient of $\xi_1 \approx 45$, somewhat smaller than for the B3LYP/CAM-B3LYP but still very large.

From the analysis so far, one may naively assume that there is a one-to-one correspondence between nodal hypersurfaces and the corresponding energies. The example of $M = 4$ multiplicity shows this not necessarily the case. ξ_1 for B3LYP/BPW91 nodal differences is ≈ 36 (i.e. much smaller than the B3LYP/CAM-B3LYP or BPW91/TPSSH nodal differences for $M = 6$), yet the B3LYP/BPW91 functionals yield almost identical QMC relative energies and energies to within ≈ 0.1 eV for $M = 4$.

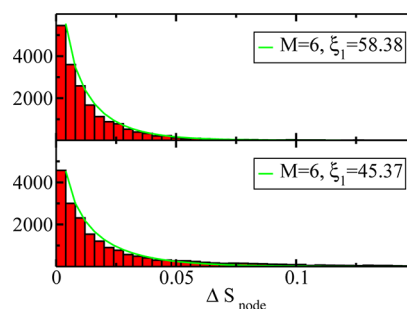


Figure 8. Distribution of the differences between B3LYP and CAM-B3LYP and TPSSH and BPW91 nodal hypersurfaces for spin multiplicity $M = 6$. The color scheme is the same as for Figure 7.

■ ASSOCIATED CONTENT

Supporting Information

Pseudopotential total energies calculated at the DFT and QMC levels along with corresponding QMC energies before structural optimization. This material is available free of charge via the Internet at <http://pubs.acs.org/>.

■ AUTHOR INFORMATION

Corresponding Author

*E-mail: ivan.stich@savba.sk.

Notes

The authors declare no competing financial interest.

■ ACKNOWLEDGMENTS

This research was supported in part by APVV-0091-07, APVV-0207-11, LPP-0392-09, and VEGA (2/0007/12) projects and via CE SAS QUTE. Further support provided by ARO, NSF, and DOE, as well as computer time allocations under Teragrid and ALCC programs, are gratefully acknowledged.

■ REFERENCES

- (1) Braga, D.; Dyson, P. J.; Grepioni, F.; Johnson, B. F. G. *Chem. Rev.* **1994**, *94*, 1585.
- (2) Ma, J. C.; Dougherty, D. A. *Chem. Rev.* **1997**, *97*, 1303.
- (3) Dougherty, D. A. *Science* **1996**, *271*, 163.
- (4) Kurikawa, T.; Takeda, H.; Hirano, M.; Judai, K.; Arita, T.; Nagao, S.; Nakajima, A.; Kaya, K. *Organometallics* **1999**, *18*, 1430.
- (5) Xiang, H.; Yang, J.; Hou, J. G.; Zhu, Q. *J. Am. Chem. Soc.* **2006**, *128*, 2310.
- (6) Mokrousov, Y.; Atodiresei, N.; Bihlmayer, G.; Heinze, S.; Blügel, S. *Nanotechnology* **2007**, *18*, 495402.
- (7) Pandey, R.; Rao, B. K.; Jena, P.; Newsam, J. A. *Chem. Phys. Lett.* **2000**, *321*, 142.
- (8) Pandey, R.; Rao, B. K.; Jena, P.; Blanco, M. A. *J. Am. Chem. Soc.* **2001**, *123*, 3799.
- (9) Kandam, A. K.; Rao, B. K.; Jena, P.; Pandey, R. *J. Chem. Phys.* **2004**, *120*, 10414.
- (10) Maslyuk, V. V.; Bagrets, A.; Meded, V.; Arnold, A.; Evers, F.; Brandbyge, M.; Bredow, T.; Mertig, I. *Phys. Rev. Lett.* **2006**, *97*, 097201.
- (11) Rudenko, A. N.; Keil, F. J.; Katsnelson, M. I.; Lichtenstein, A. I. *Phys. Rev. B* **2012**, *86*, 075422.
- (12) Sargolzaei, M.; Gudarzi, F. *J. Appl. Phys.* **2011**, *110*, 064303.
- (13) Binz, S. M.; Hupalo, M.; Liu, X.; Wang, C. Z.; Lu, W.-C.; Thiel, P. A.; Ho, K. M.; Conrad, E. H.; Tringides, M. C. *Phys. Rev. Lett.* **2012**, *109*, 026103.
- (14) Horváthová, L.; Dubecký, M.; Mitas, L.; Štich, I. *Phys. Rev. Lett.* **2012**, *109*, 053001.
- (15) Parr, R. G.; Yang, W. *Density-Functional Theory of Atoms and Molecules*; University Press: New York, 1994; pp 142–201.

- (16) Grossman, J. C.; Mitas, L.; Raghavachari, K. *Phys. Rev. Lett.* **1995**, *75*, 3870.
- (17) Hongo, K.; Watson, M. A.; Sanchez-Carrera, R. S.; Iitaka, T.; Aspuru-Guzik, A. *J. Phys. Chem. Lett.* **2010**, *1*, 1789.
- (18) Kolorenc, J.; Mitas, L. *Phys. Rev. Lett.* **2008**, *101*, 185502.
- (19) Kolorenc, J.; Mitas, L. *Phys. Rev. B* **2010**, *82*, 115108.
- (20) Duncan, M. A. *Int. J. Mass Spectrom.* **2008**, *272*, 99.
- (21) Hathout, Y.; Fabris, D.; Fenselau, C. *Int. J. Mass Spectrom.* **2001**, *204*, 1.
- (22) Jaeger, T. D.; van Heijnsbergen, D.; Klippenstein, S. J.; von Helden, G.; Meijer, G.; Duncan, M. A. *J. Am. Chem. Soc.* **2004**, *126*, 10981.
- (23) Meyer, F.; Khan, F. A.; Armentrout, P. B. *J. Am. Chem. Soc.* **1995**, *117*, 9740.
- (24) Hettich, R. L.; Jackson, T. C.; Stanko, E. M.; Freiser, B. S. *J. Am. Chem. Soc.* **1986**, *108*, 5086.
- (25) Miyajima, K.; Yabushita, S.; Knickelbein, M. B.; Nakajima, A. *J. Am. Chem. Soc.* **2007**, *129*, 8473.
- (26) Yang, C.-N.; Klippenstein, S. J. *J. Chem. Phys. A* **1999**, *103*, 1094.
- (27) Bauschlicher, C. W., Jr.; Partridge, H.; Langhoff, S. R. *J. Phys. Chem.* **1992**, *96*, 3273.
- (28) Rabilloud, F. *J. Phys. Chem.* **2005**, *122*, 134303.
- (29) Polestshuk, P. M.; Dem'yanov, P. I.; Ryabinkin, I. G. *J. Phys. Chem.* **2008**, *129*, 054307.
- (30) Wildberger, K.; Stepanyuk, V. S.; Lang, P.; Dederichs, P. J. *Phys. Rev. Lett.* **1995**, *75*, 509.
- (31) Staroverov, V. N.; Scuseria, G. N.; Tao, J.; Perdew, J. P. *J. Chem. Phys.* **2003**, *119*, 12129.
- (32) Staroverov, V. N.; Scuseria, G. N.; Tao, J.; Perdew, J. P. *J. Chem. Phys.* **2004**, *121*, 11507.
- (33) Schwabe, T.; Grimme, S. *Phys. Chem. Chem. Phys.* **2007**, *9*, 3397.
- (34) Foulkes, W. M. C.; Mitas, L.; Needs, R. J.; Rajagopal, G. *Rev. Mod. Phys.* **2001**, *73*, 33.
- (35) Bajdich, M.; Mitas, L. *Acta Phys. Slovaca* **2009**, *59*, 81.
- (36) Schmidt, M. V.; Baldrige, K. K.; Boatz, J. A.; Elbert, S. T.; Gordon, M. S.; Jensen, J. H.; Koseki, S.; Matsunaga, N.; K. A. Nguyen, K. A.; Su, S.; et al. *J. Comput. Chem.* **1993**, *14*, 1347.
- (37) Gordon, S.; Schmidt, M. W. In *Theory and Applications of Computational Chemistry: The First Forty Years*; Dykstra, C. E., Frenking, G., Kim, K. S., Scuseria, G. E., Eds.; Elsevier: Amsterdam, **2005**; pp 1167–1189.
- (38) Wagner, L.; Bajdich, M.; Mitas, L. *J. Comput. Phys.* **2009**, *228*, 3390.
- (39) Becke, A. D. *Phys. Rev. A* **1988**, *38*, 3098.
- (40) Perdew, J. P.; Wang, Y. *Phys. Rev. A* **1988**, *38*, 3098.
- (41) Becke, A. D. *J. Chem. Phys.* **2009**, *228*, 3390.
- (42) Stephens, P. J.; Delvin, F. J.; Chabalowski, C. F.; Frisch, M. J. *J. Phys. Chem.* **1994**, *98*, 11623.
- (43) Yanai, T.; Tew, D.; Handy, N. *Chem. Phys. Lett.* **2004**, *393*, 51.
- (44) Grimme, S.; Neese, F. *J. Chem. Phys.* **2007**, *127*, 154116.
- (45) Perdew, J. P.; Burke, K.; Ernzerhof, M. *Phys. Rev. Lett.* **1996**, *77*, 3865.
- (46) Perdew, J. P.; Burke, K.; Ernzerhof, M. *Phys. Rev. Lett.* **1997**, *78*, 1396.
- (47) Greeff, C.; Lester, J. W. A. *J. Chem. Phys.* **1998**, *109*.
- (48) Ovcharenko, I.; Aspuru-Guzik, A.; Lester, J. W. A. *J. Chem. Phys.* **2001**, *114*, 7790.
- (49) Dunning, J. T. H. *J. Chem. Phys.* **1989**, *90*, 1007.
- (50) Schmidt, K. E.; Moskowitz, J. W. *J. Chem. Phys.* **1990**, *93*, 4172.
- (51) Filippi, C.; Umrigar, C. J. *Phys. Rev. Lett.* **2005**, *94*, 150201.
- (52) Wagner, L.; Mitas, L. *Chem. Phys. Lett.* **2003**, *370*, 412.
- (53) Balabanov, N. B.; Peterson, K. J. *J. Chem. Phys.* **2006**, *125*, 074110.
- (54) Raghavachari, K.; Trucks, G. W. *J. Chem. Phys.* **1989**, *91*, 2457.
- (55) Sansonetti, J. E.; Martin, W. C. *J. Phys. Chem. Ref. Data* **2005**, *34*, 1559.
- (56) Osanai, Y.; Ishikawa, H.; Miura, N.; Noro, T. *Theor. Chem. Acc.* **2001**, *105*, 437.
- (57) Dubecký, M.; Derian, R.; Mitas, L.; Štich, I. *J. Chem. Phys.* **2010**, *133*, 244301.
- (58) Dubecký, M.; Derian, R.; Horváthová, L.; Allan, M.; Štich, I. *Phys. Chem. Chem. Phys.* **2011**, *13*, 20939.
- (59) Bauschlicher, C. W., Jr.; Langhoff, S. R.; Partridge, H.; Barnes, L. A. *J. Phys. Chem.* **1989**, *91*, 2399.
- (60) Raghavachari, K.; Trucks, G. W. *J. Chem. Phys.* **1989**, *91*, 1062.